Master in Quantum Science and Technology Barcelona

ICN2 Institut Català de Nanociència i Nanotecnologia

Spin dynamics in heterostructures composed of ferroelectric van der Waals semiconductors and graphene

Gabriel de Araújo Masanti

Supervised by: ICREA Prof. Sergio O. Valenzuela & Dr. Juan F. Sierra

Institut Català de Nanociència i Nanotecnologia, UAB Campus, 08193 Bellaterra, Barcelona

7 July 2025

Spintronics is a field that harnesses the spin degree of freedom of electrons to store, process, and transmit information. Van der Waals heterostructures combining graphene and high spin orbit coupling 2D materials are a promising platform to control spin transport, where proximity-induced effects change the behaviour of spin relaxation in graphene giving rise to spin lifetime anisotropy. In this work we study devices made of graphene and $CuInP_2S_6$ (CIPS), demonstrated to be a ferroelectric material in the few layers limit, with the goal of controlling spin transport properties in graphene by means of electric fields. We demonstrate that charge transport in graphene can be tuned by altering the ferroelectric state of CIPS, and we observe spin-lifetime anisotropy in graphene. Furthermore, we explore the potential of controlling the strength of this anisotropy through ferroelectric modulation.

Keywords: 2D materials, van der Waals heterostructures, proximity effects, spin precession, anisotropic spin dynamics

Gabriel de Araújo Masanti: gabriel.dearaujo@icn2.cat

Acknowledgements

This Master Thesis was a great experience, especially because of the great scientists and human beings that I met along the way.

First of all, I would like to deeply thank Sergio O. Valenzuela for letting me conduct both my Internship and Master Thesis in his group, having the opportunity to delve into experimental physics in one of the leading groups in the field. Besides, I really appreciate the insightful discussions that we shared about fundamental physical phenomena.

I also need to express my immense gratitude to Juan F. Sierra, who taught me all I needed to know, from fabrication, to measurements and results discussion. Thank you for always being available to talk, for your passion, and for the way you share it with others. I truly admire how you encourage and motivate people to excel in a very heartfelt way, and you always offer your support when needed. Your ability to explain complex concepts with simplicity and to teach by asking thought-provoking questions has deeply inspired me. Your enthusiasm is what initially drew me to the group, and it continues to inspire me every day.

I would like to thank Patricia for the support she has given me, always ready to help and teach, both in the lab and with experimental setups. Thank you for your patience during the preparation of my devices, often prioritizing my work over your own. I am sincerely grateful for that.

I would like to thank also the whole group, since they are really kind and open to help, and they have made me feel at home. Thanks to Biel, Mireia and Cata for all the days shared in the lab. Thanks to Enzo, Motomi, Nandan and Carme for welcoming me warmly to the office, also helping when needed. Thanks to Josef and Franz for all the discussions and support.

Finally, and most importantly, I would like to profoundly thank Sonia, who brought me the most unconditional support in a daily basis. I am certain that I wouldn't be where I am today without you. You bring out the best in me in every way, encouraging me to reach for all that I aspire to achieve. Thank you for the endless support, joy, and love you always give me.

Contents

1 Introduction

1.1 Spintronics

Spin electronics, commonly known as spintronics, seeks to control the spin degree of freedom of electrons in condensed matter systems to manipulate, store, and transmit information and it has emerged as a promising route to reduce energy dissipation in electronic devices.

Magnetic regions, made of an arrangement of spins, have been used to store information since the 19th century [DMG98]. From hard disk drives [HJ70] with magnetoresistive read head, to giant magnetoresistance [BBF+88, BGSZ89] and many other phenomena, the field has advanced significantly, enabling breakthroughs in data storage and magnetic sensing, and bringing promising architectures for spin-based logic. These developments have laid the foundation for modern spintronic technologies, where electron spin is actively exploited to achieve functionalities beyond the reach of conventional charge-based electronics.

Ultra-low energy operation can be achieved by exploiting the recently proposed magnetoelectric spin-orbit logics [MNL+18], paving the way for the development of reconfigurable energy-efficient spintronic devices.

Nonetheless, most materials are not suitable for the transmission of information, since spins suffer fast decoherence resulting in loss of information.

1.2 Graphene spintronics and proximity effects

The most promising candidate is graphene [NGM+04], since it has a weak spin-orbit coupling (SOC), reducing the mechanisms of spin relaxation, it presents minimal hyperfine interactions, a major source of decoherence, and it has a high carrier mobility, with electrons behaving as massless Dirac fermions. Although this ensures a long spin lifetime [DFV+16, GPS+19], the weak spin-orbit coupling in graphene precludes efficient spin manipulation, limiting its role to that of an interconnect. Spin-orbit coupling is a fundamental quantum mechanical interaction between the spin of an electron and its motion, leading to coupling between spin and momentum and offering powerful ways to control spin using electric fields or structural asymmetries.

On the other hand, other 2D materials have been recently studied since the isolation of graphene [BLM+15], exploring van der Waals heterostructures with the goal of imprinting spin-orbit coupling onto graphene through proximity effects [SFK+21].

Van der Waals heterostructures are artificially stacked layers of 2D materials, held together by weak van der Waals forces. In these heterostructures, there are short-range interactions across their interface where a material induces a property in another material, called proximity effects [ŽMAS+19].

In recent studies, spin lifetime anisotropy was achieved assembling heterostructures by placing transition metal dichalcogenides on top of graphene [BSST+17, HSIA+20, SSST+25]. These materials have strong spin-orbit coupling that imprints anisotropy in the spin dynamics in graphene, which for some cases can be modified through a back-gate voltage. However, the modulation of anisotropy is not retained after the gate voltage is removed.

This thesis investigates the control of spin dynamics using ferroelectric materials. Characterized by nonvolatile internal electric fields, these materials have the potential to modulate SOC in graphene through proximity effects. In recent years several van der Waals materials have been identified with ferroelectric properties. The polarization of these materials can be switched by an applied top-gate voltage modifying, in principle, the interactions with graphene.

In this work, $CuInP_2S_6$ (CIPS) is used with the stated objective.

1.3 $CuInP_2S_6$, a 2D ferroelectric material

CIPS is one of the few layered materials that presents room-temperature ferroelectricity [SRM+94] in the ultrathin limit [LYS+16] showing an out-of-plane polarization [MCS+97].

The atomic structure of CIPS consists of a sulfur framework, with octahedral voids occupied by Cu, In, and P-P triangular units, which can be seen in Fig. 1.

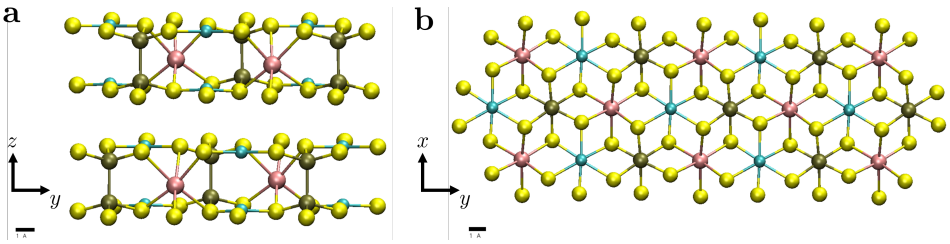

Figure 1: **CIPS structure. a.** Two adjacent monolayers are needed to describe CIPS symmetry due to the site exchange between Cu and P-P. **b.** Top view where triangular patterns can be seen.

The Curie temperature of CIPS is ∼315 K [SRM+94], when a spontaneous out-of-plane polarization appears in the ferrielectric phase due to off-center ordering of Cu atoms and displacement of In cations, causing a symmetry change from $C_{2/c}$ (centrosymmetric) to C_c (non-centrosymmetric). The direction of polarization corresponds to the z axis in Fig. 1. Furthermore, the polarization of this material can be reliably switched using a bias voltage [LYS+16], motivating its use.

All in all, CIPS becomes a promising material to investigate in proximitized devices for spintronics.

2 Theoretical background

2.1 Hamiltonian

To understand the behaviour of these heterostructures, we have to know the interactions that are taking place. For this, we will discuss all the contributions to the Hamiltonian, going from isolated graphene to the heterostructure identifying the key differences.

2.1.1 Graphene

The Hamiltonian describing electrons in pristine graphene can be described by the massless Dirac fermions term near the K and K' points:

$$H_0 = \hbar v_F(\kappa k_x \sigma_x - k_y \sigma_y), \tag{1}$$

where $\hbar$ is Planck constant, v_F is the Fermi velocity, κ is the valley index with value $+1$ (-1) for K (K'), $\vec{k}$ is the wave vector and $\sigma_{0,x,y,z}$ are the sublattice pseudospin Pauli matrices. This gives graphene the usual linear dispersion relation and the corresponding Dirac cones.

Due to its weak intrinsic spin orbit coupling, graphene is the material with the longest spin diffusion length and spin lifetime, making it ideal as an interconnect for spin transport

[SFK+21]. Nevertheless, its weak spin orbit coupling, of magnitude $\lambda_I \sim 12$ μeV [GF15], it is not suitable for spin control. This term opens a gap of $2\lambda_I$ from the following contribution

$$H_I = \lambda_I \kappa \sigma_z s_z, \tag{2}$$

where $s_{0,x,y,z}$ are the spin Pauli matrices.

Moreover, graphene is usually placed on substrates, stabilizing it and decreasing its thermal fluctuations. This breaks the out-of-plane inversion symmetry, coupling spin and in-plane momentum and leading to spin splitting. This can be described by the Rashba spin orbit coupling term

$$H_R = \lambda_R(\kappa \sigma_x s_y - s_y \sigma_x), \tag{3}$$

with λ_R the strength of the interaction. Additionally, space-inversion symmetry can be broken by applying an electric field or by stacking 2D materials in heterostructures, also causing Rashba spin orbit coupling.

2.1.2 Proximitized graphene

One way to overcome weak spin orbit coupling is by designing van der Waals heterostructures, layered structures built by stacking atomically thin 2D materials. In these systems, proximity-induced effects, caused by hybridization of electronic orbitals and tunneling between adjacent layers, can imprint useful properties on pristine graphene, potentially enabling manipulation of the spin relaxation [SFK+21, ŽMAS+19, GF15].

Spin orbit coupling proximity effects decay exponentially with the distance from the interface, therefore van der Waals heterostructures enhance them originating noticeable changes in their properties, predicted by several first-principles studies [GKE+09, GF15, GKHF16, ZJNF23, ZKGF25].

As a result, the Hamiltonian in proximited graphene will have additional contributions that will modify the low energy term H_0. Since heterostrucures are made, inversion symmetry is broken producing Rashba spin orbit coupling H_R. Besides, this term is further enhanced when having graphene combined with materials with strong intrinsic spin orbit coupling.

Furthermore, when materials with different elements breaking inversion symmetry (see Fig. 1 **b.**) are placed on top of graphene, the two sublattices (A and B) will feel different electrostatic potentials, breaking pseudospin symmetry. This results in an orbital gap opening described by the staggered potential [GF15]

$$H_\Delta = \Delta \sigma_z. \tag{4}$$

The pseudospin symmetry breaking will affect also the intrinsic spin orbit coupling experienced by each sublattice, modifying the corresponding contribution $(\lambda_I^A, \lambda_I^B)$ as follows:

$$H_I = \frac{1}{2}\left[\lambda_I^A(\sigma_z + \sigma_0) + \lambda_I^B(\sigma_z - \sigma_0)\right]\kappa s_z. \tag{5}$$

Moreover, new spin orbit coupling terms emerge due to the pseudospin inversion asymmetry (PIA) [GKF13, GKHF16] capturing a k linear band splitting and spin flip:

$$H_{PIA} = \frac{a}{2}\left[\lambda_{PIA}^A(\sigma_z + \sigma_0) + \lambda_{PIA}^B(\sigma_z - \sigma_0)\right](k_x s_y - k_y s_x), \tag{6}$$

with $\lambda_{PIA}^A, \lambda_{PIA}^B$ the strength in each sublattice, and a the lattice constant of graphene.

In addition, these type of heterostructures can break time-reversal symmetry locally in k-space, generating a valley dependent spin-splitting, called valley-Zeeman, of strength λ_{VZ} [SFK+21]:

$$H_{VZ} = \lambda_{VZ}\kappa s_z. \tag{7}$$

Overall, energy bands in proximitized graphene can be described near K and K' points as

$$H = H_0 + H_\Delta + H_I + H_R + H_{PIA} + H_{VZ} \tag{8}$$

2.2 Spin transport

Now that we have the contributions to the Hamiltonian, we discuss how the spins flow in graphene.

Besides charge, electrons have spin as an additional degree of freedom. When injecting charge current $\vec{J}_c$, electrons may have different spin polarization. In the two spin channel model of conduction, the charge current has contributions of both spin up ($\vec{J}_\uparrow$) and spin down ($\vec{J}_\downarrow$) polarized currents, namely

$$\vec{J}_c = \vec{J}_\uparrow + \vec{J}_\downarrow. \tag{9}$$

On the other hand, we can define a pure spin current that accounts for the imbalance in both spin polarized currents:

$$\vec{J}_s = \vec{J}_\uparrow - \vec{J}_\downarrow. \tag{10}$$

In non-magnetic materials both spin up and spin down currents are equal, since there is no preferential spin polarization, resulting in a zero spin current. Nonetheless, ferromagnetic materials may present a spin-polarized current because of the imbalance in the density of states for spin up and spin down carriers. Since non-magnetic materials have a spin-independent conductivity we can write

$$\vec{J}_{\uparrow(\downarrow)} = -\frac{\sigma}{2e}\nabla\vec{\mu}_{\uparrow(\downarrow)}, \tag{11}$$

where σ is the electrical conductivity of the non-magnetic channel.

Hence, we can express the pure spin current as

$$\vec{J}_s = -\frac{\sigma}{2e}\nabla(\vec{\mu}_\uparrow - \vec{\mu}_\downarrow) = -\frac{\sigma}{2e}\nabla\vec{\mu}_s. \tag{12}$$

This means that the driving force for the spin current is the gradient of the spin accumulation $\vec{\mu}_s$ [MVSK17].

2.3 Spin valve lateral device configuration

To study proximity effects in the heterostructures designed in this work, we have to be able to inject and detect spin polarized current propagating in the graphene plane. For this, we will use the device geometry called non-local lateral device, proposed by Johnson and Silsbee [JS88b, JS85]. These type of devices can be used in non-local measurements where the injection and detection region are spatially separated, i.e. the charge current does not flow through the detector electrodes. Non-local measurements are useful to eliminate [VT06] or reduce [VBS+22] spurious effects due to anisotropic magnetoresistance in the ferromagnetic electrodes or the Hall effect, making them mainly sensitive to pure spin currents.

In Fig. 2 **a.** we can see the geometry of the devices, where the graphene flake is connected by two non-magnetic and two ferromagnetic electrodes. The graphene channel

has a width W and a length L, the latter being the distance between the ferromagnetic electrodes. These ferromagnetic electrodes are built as thin and narrow strips to have their easy axis of magnetization along the long axis due to shape anisotropy. Moreover, each ferromagnet has a different width so that they have different coercive fields, enabling the preparation of the parallel and antiparallel relative configurations of their magnetization applying a magnetic field along the easy axis.

On the other hand, the conductivity of graphene is considerably smaller than that of ferromagnetic contacts. Consequently, there would be spin absorption to the ferromagnetic electrode due to the impedance mismatch, reducing the spin injection [SFM+00]. To overcome this issue, ferromagnetic electrodes are usually prepared with a tunnel barrier at the interface [Ras00, JHF+02]. Several tunnel barriers had been used in graphene devices such as Al_2O_3 [TJP+07], but in this work we employed TiO_x beneath Co ferromagnetic electrodes as in previous studies [SNC+17].

Since the ferromagnets have different density of states for spin up and spin down electrons, charge current flowing through a ferromagnet will be spin polarized. This conversion between charge and spin current is described by an effective polarization of the injector electrode

$$\vec{J}_s = P_i \vec{J}_c, \tag{13}$$

which depends on the relative difference between spin up and spin down density of states, the quality of the tunnel barrier, the voltage applied, etc.

As we have seen, a current is related to a gradient in electrochemical potential which will diffuse obeying the 1D diffusion equation

$$\nabla^2 \vec{\mu}_s = \frac{1}{\lambda_s^2} \vec{\mu}_s, \tag{14}$$

under the assumption of $L \gg W$, and λ_s being the spin diffusion length.

This electrochemical potential gradient results in a spin accumulation underneath the detector at a distance L with a corresponding non-local voltage along the magnetization direction of magnitude

$$V_{\text{nl}} = \frac{P_d}{2} \mu_s^y(L), \tag{15}$$

with $\mu_s^y(x) = \mu_0^s e^{-x/\lambda_s}$ after applying boundary conditions. This non-local voltage is related to a non-local resistance $R_{\text{nl}} = V_{\text{nl}}/I$, the magnitude that we will study.

This resistance can be measured while sweeping the magnetic field along the direction of magnetization, i.e. the easy axis of the ferromagnetic electrodes. Consequently, there will be switchings from $+R_{\text{nl}}$ to $-R_{\text{nl}}$ corresponding to the relative magnetization of the ferromagnetic electrodes going from parallel to antiparallel, respectively, as seen in Fig. 2 **c** and **d**. This difference in resistance gives us the magnitude of the spin signal ΔR_{nl}. Notice that in Fig. 2 **d** there are extra switchings due to the fact that the device was measured using four ferromagnetic electrodes [TJP+07].

2.4 Hanle spin precession in pristine graphene

The determination of the spin lifetimes is typically achieved by performing Hanle spin precession measurements. These experiments consist of applying a magnetic field perpendicular to the graphene plane causing the injected spins to precess in-plane as they diffuse. The magnetic field $\vec{B}$ applied exerts a torque on the injected spins $\vec{\mu}_s$, which precess with a given Larmor frequency. The torque is given by

$$\vec{\tau} = \gamma_c \vec{\mu}_s \times \vec{B}, \tag{16}$$

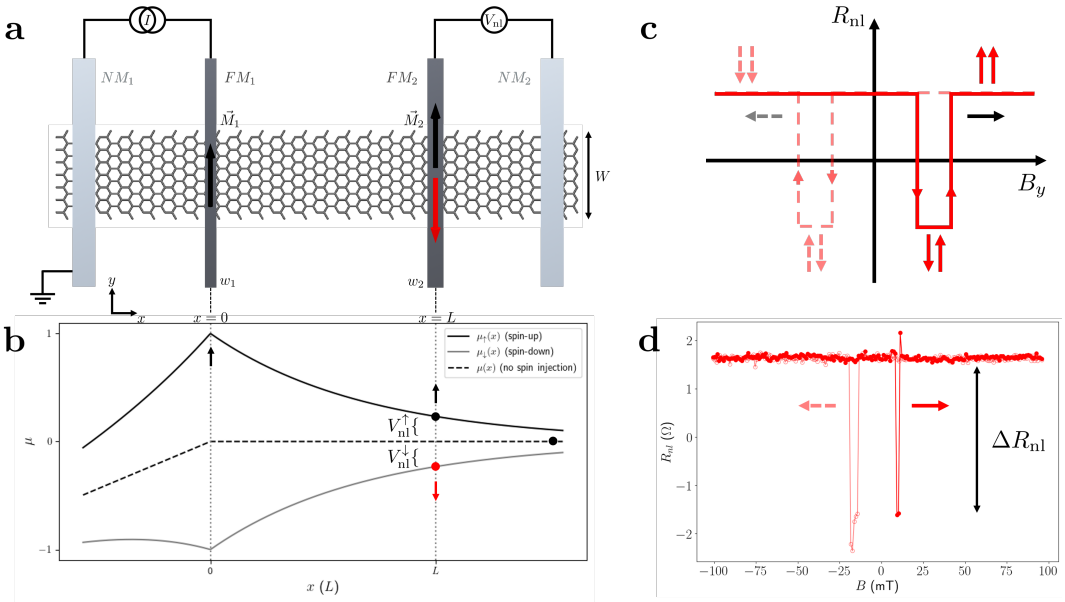

Figure 2: **Non-local device geometry. a.** Spin valve lateral device in a non-local configuration. **b.** Electrochemical potential beneath the electrodes. **c.** Non-local measurement sweeping the magnetic field in the direction of the ferromagnetic contacts. **d.** Experimental data showing the switchings of the ferromagnets and the magnitude of the spin signal.

where γ_c is the gyromagnetic ratio. In the case of electrons, the gyromagnetic ratio is

$$\gamma_c = \frac{e g_e}{2 m_e} \overset{g_e \simeq 2}{=} \frac{e}{m_e}, \tag{17}$$

with e, g_e and m_e the charge, the g-factor and the mass of the electron, respectively. The Larmor frequency is therefore $\omega_L = \gamma_c |\vec{B}|$.

Hence, in the devices used spins are injected at the ferromagnetic contacts, they diffuse through the channel, they precess due to the magnetic field applied and they also relax. Thus, to model spin dynamics we will use the 1D Bloch diffusion equation

$$\frac{\partial}{\partial t}\vec{\mu}_s = D_s \frac{\partial^2}{\partial x^2}\vec{\mu}_s - \gamma_c \vec{\mu}_s \times \vec{B} - \tau_s^{-1}\vec{\mu}_s, \tag{18}$$

where we introduced a spin diffusion constant D_s, and the relaxation time τ_s.

Notice that the third term is the torque exerted by the magnetic field $\vec{B}$ which describes the spin precession, while the fourth term models the spin relaxation.

In the high contact resistance regime, neglecting the relaxation processes induced by the contact, we can express the non-local spin signal when applying a perpendicular magnetic field as [JHF+02]

$$R_{\rm nl}(B) = \pm \frac{P_i P_d}{e^2 N(E_F) W} \int_0^\infty \frac{1}{\sqrt{4\pi D_s t}} \exp\left(-\frac{L^2}{4 D_s t}\right) \cos(\omega_L t) \exp\left(-\frac{t}{\tau_s}\right) dt, \tag{19}$$

since it is related to the spin accumulation at the detector, as derived in Appendix A.1. Here $\pm$ corresponds to parallel and antiparallel relative configurations of the ferromagnetic contacts. The first term $\frac{1}{\sqrt{4\pi D_s t}} \exp\left(-\frac{L^2}{4 D_s t}\right)$ accounts for the distribution of the spins that arrive to the detector at a certain time t. The second term $\cos(\omega_L t)$ is the projection of the spins along the magnetization of the detector and accounts for Larmor precession.

The third term $\exp(-t/\tau_s)$ describes the spin relaxation. In this way, we can extract the desired spin dynamics parameters τ_s, D_s, λ_s and $P_i P_d$ by fitting the experimental data to the analytical expression in Eq.(19).

In Fig. 3 we can see a scheme of the spin precession in a graphene spin valve and the corresponding Hanle curve. This curve is symmetric due to isotropic in-plane spin lifetimes, it has a maximum at zero magnetic field due to the alignment of the diffused spins and the magnetization of the detector, and it has two minima at $\pm B_{\text{min}}$ where spins precess such that they arrive to the detector antiparallel to its magnetization. Above $\pm B_{\text{dp}}$, spins fully dephase giving zero signal. The value of B_{dp} depends on the length of the channel and the spin parameters (diffusion and lifetime) in graphene. For longer channels spins travel more and need lower fields to dephase completely.

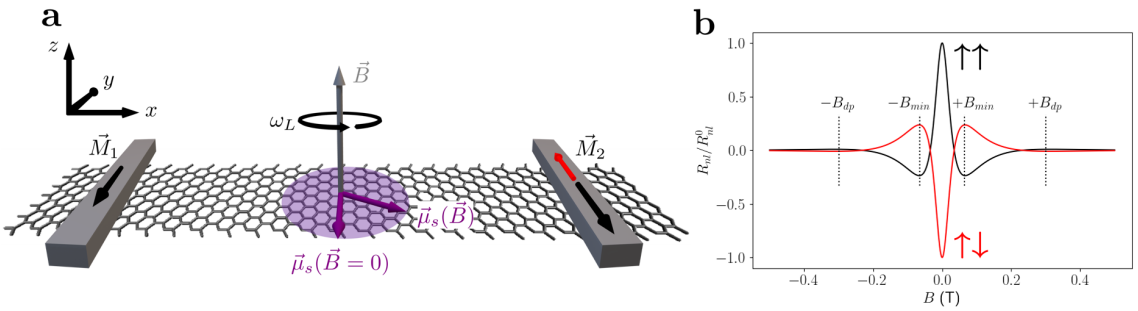

Figure 3: **Hanle spin precession. a.** Spin in-plane precession in graphene spin valve device. **b.** Analytical Hanle curves for both parallel and antiparallel configurations of the injector and the detector.

2.5 Tilting of the ferromagnetic contacts

Due to the applied magnetic field, the magnetization of the cobalt ferromagnetic contacts starts to rotate, modifying the expected Hanle precession curve. In thin ferromagnetic cobalt electrodes the out-of-plane magnetization saturation field is high enough such that the analytical curves fit the experimental data. However, fittings can be improved by taking into account the tilting of the ferromagnetic contacts, important for shorter graphene channels, where larger magnetic fields need to be applied to reach B_{dp}.

The tilt angle γ of the magnetization of the ferromagnetic electrodes can be related to the angle β in which magnetic field is applied. The angle β lies in the yz plane and is measured from the y axis (direction of the ferromagnets), being $\beta = 90°$ in Fig. 3. To do so, we use the Stoner-Wohlfarth model [TG08, SW48], where the tilting takes the form

$$\gamma = \arcsin\left(\frac{B\sin\beta}{B_s + B\cos\beta}\right). \tag{20}$$

This angle can be introduced to improve the analytical expression of the non-local resistance taking into account the projections of the magnetization onto the contacts in the following way

$$R^*_{\text{nl}}(B) = R_{\text{nl}}(B)\cos^2\gamma + R^0_{\text{nl}}\sin^2\gamma, \tag{21}$$

where R^0_{nl} is the resistance at zero magnetic field.

In Fig. 4 we can see how the rotation in the magnetization affects the Hanle precession curve. Since the tilting angle γ increases with the magnetic field applied, the non-precessing component of the spin current also increases.

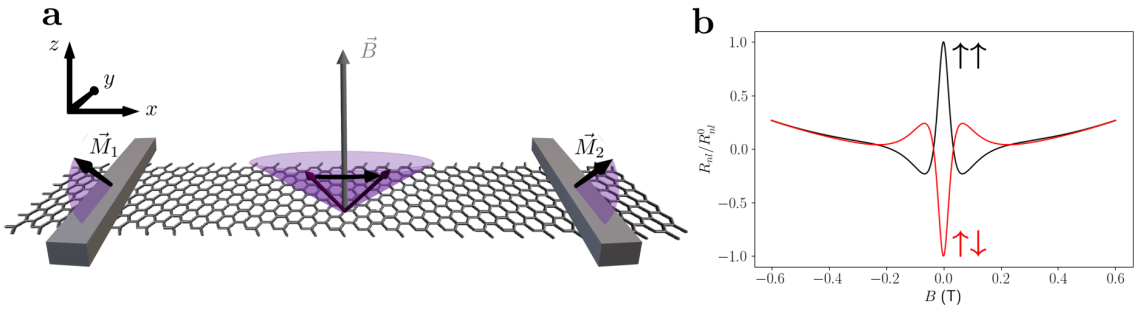

Figure 4: **Tilting of the ferromagnetic electrodes. a.** Spin precession in graphene spin valve device taking into the account the tilting in the magnetization of the ferromagnetic contacts. **b.** Corresponding analytical Hanle curves for both parallel and antiparallel configurations of the injector and the detector.

2.6 Proximitized spin valve lateral devices

Up to this point we assumed isotropic spin relaxation lifetimes, resulting in equal τ_s for all directions. Nevertheless, spin dynamics can be anisotropic, especially in heterostructures, giving rise to different spin lifetimes τ_x^s, τ_y^s and τ_z^s and providing insights about the spin orbit fields relevant in the relaxation.

Thus, applying an out-of-plane magnetic field, spins precess in-plane, giving us information about τ_x^s and τ_y^s. To understand the spin dynamics out-of-plane one could think to apply a magnetic field parallel to the channel. However, the in-plane saturation field deviates from the Stoner-Wohlfarth model, being much lower and causing a discrepancy between the experimental data and the analytical expression. Hence, we will use a different approach.

2.7 Oblique spin precession

The scheme used in this work to study anisotropic spin transport is the one proposed in [RSC+16]. In the heterostructures studied, we expect the spin orbit field to be out-of-plane, since the polarization of CIPS will modify the Rashba interaction, which is in-plane. Then, we assume that the spin dynamics in-plane is isotropic, i.e. $\tau_x^s = \tau_y^s \coloneqq \tau_\parallel^s$, and we define $\tau_z^s \coloneqq \tau_\perp^s$.

To estimate the spin anisotropy $\zeta = \tau_\perp^s/\tau_\parallel^s$ we can simplify Eq.(18) for the limiting case in which the precession is fully dephased . In this scenario, the component perpendicular to the magnetic field dies away leaving only the component along the magnetic field direction $\hat{B}$. Projecting the spin electrochemical potential onto the direction of $\vec{B}$ we have

$$\mu_{B_\parallel}^s = \vec{\mu}_s \cdot \hat{B} = \mu_y^s \cos\beta + \mu_z^s \sin\beta, \tag{22}$$

since we apply the magnetic field in the yz plane.

Taking into account that we expect the system to present anisotropy between in-plane and out-of-plane spin lifetimes we can write

$$\begin{aligned} \frac{\partial}{\partial t}\mu_y^s &= D_s \frac{\partial^2}{\partial x^2}\mu_y^s - (\tau_\parallel^s)^{-1}\mu_y^s \\ \frac{\partial}{\partial t}\mu_z^s &= D_s \frac{\partial^2}{\partial x^2}\mu_z^s - (\tau_\perp^s)^{-1}\mu_z^s. \end{aligned} \tag{23}$$

If we differentiate Eq.(22) and we plug it in Eq.(23) we obtain

$$\frac{\partial}{\partial t}\mu_{B_\parallel}^s = \cos\beta \left(D_s \frac{\partial^2}{\partial x^2}\mu_y^s - (\tau_\parallel^s)^{-1}\mu_y^s \right) + \sin\beta \left(D_s \frac{\partial^2}{\partial x^2}\mu_z^s - (\tau_\perp^s)^{-1}\mu_z^s \right) \tag{24}$$

Now we can assume that spin remains aligned with $\vec{B}$ during its decay, and that the transverse components are dephased, giving $\mu_y^s \simeq \mu_{B_\parallel}^s \cos\beta$ and $\mu_z^s \simeq \mu_{B_\parallel}^s \sin\beta$. Hence, Eq.(24) can be written as

$$\frac{\partial}{\partial t}\mu_{B_\parallel}^s = D_s \frac{\partial^2}{\partial x^2}\mu_{B_\parallel}^s - (\tau_\beta^s)^{-1}\mu_{B_\parallel}^s, \tag{25}$$

with

$$(\tau_\beta^s)^{-1} = (\tau_\parallel^s)^{-1}\left(\cos^2\beta + \frac{1}{\zeta}\sin^2\beta\right) \tag{26}$$

In the steady state, the solution to Eq.(25) is known and the non-local spin resistance in the detector at a distance L is of the form [RSC+16, JHF+02, JS88a]

$$R_{\rm nl}^\beta = \alpha\sqrt{\frac{\tau_\beta^s}{D_s}}e^{-\sqrt{\frac{L^2}{\tau_\beta^s D_s}}}\cos^2(\beta-\gamma), \tag{27}$$

where α depends on the sheet resistance of graphene and on the polarization of the ferromagnetic contacts. The factor $\cos^2(\beta-\gamma)$ is a correction due to the tilting, given by the angle γ, in the magnetization of both the ferromagnetic injector and detector to the projection along the magnetic field. Here we assumed that both contacts behaved the same when tilting. Normalizing to the value at $\vec{B}=0$, and neglecting magnetoresistance effects $(\alpha(\vec{B})/\alpha(0)=1)$ we obtain

$$\frac{R_{\rm nl}^\beta}{R_{\rm nl}^0} = \sqrt{\frac{\tau_\beta^s}{\tau_\parallel^s}}\exp\left[-\sqrt{\frac{L^2}{\tau_\parallel^s D_s}}\left(\sqrt{\frac{\tau_\parallel^s}{\tau_\beta^s}}-1\right)\right]\cos^2(\beta-\gamma). \tag{28}$$

Combining Eq.(26) and Eq.(28) we can determine the value of ζ by plotting $R_{\rm nl}^\beta/R_{\rm nl}^0$ against $\cos^2(\beta-\gamma)$.

The behaviour of the signal depending on the anisotropy ζ following Eq. (28) can be seen in Fig. 5. When $\zeta > 1$ the curve falls above the straight line corresponding to $\zeta = 1$, while if $\zeta < 1$ it falls below it.

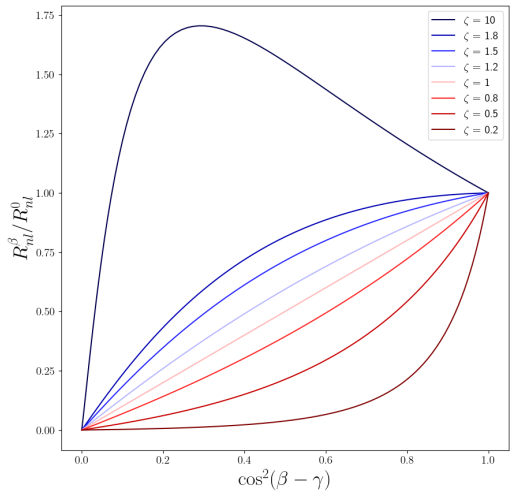

Figure 5: **Non-local resistance dependence on anisotropy ratio, ζ.** Non precessing spin component $R_{\rm nl}^\beta$ as a function of $\cos^2(\beta-\gamma)$ for different values of ζ.

3 Anisotropic spin dynamics

In the experimental design described, we will study the spin dynamics taking into account both spin diffusion and spin precession. Here we will introduce the basic equations to understand anisotropic spin dynamics and to extract the parameters of the system, such as the spin lifetimes and the anisotropy ratio.

As discussed above, to model spin dynamics we will use the steady state 1D Bloch diffusion equation

$$D_s \frac{\partial^2}{\partial x^2}\vec{\mu}_s - \gamma_c \vec{\mu}_s \times \vec{B} - \overline{\tau_s^{-1}}\vec{\mu}_s = 0, \tag{29}$$

where $\vec{\mu}_s$ is the spin electrochemical potential, D_s is the spin diffusion constant, γ_c is the gyromagnetic ratio, $\vec{B}$ is the applied magnetic field and $\overline{\tau_s^{-1}}$ is the matrix with the spin relaxation times in the diagonal

$$\overline{\tau_s^{-1}} = \begin{pmatrix} (\tau_x^s)^{-1} & 0 & 0 \\ 0 & (\tau_y^s)^{-1} & 0 \\ 0 & 0 & (\tau_z^s)^{-1} \end{pmatrix}. \tag{30}$$

Since we expect to have anisotropy between the in-plane and the out-of-plane spin lifetimes we will apply the magnetic field $\vec{B}$ in the yz plane in a certain direction given by the angle β from the y axis, i.e. $\vec{B} = B(0, \cos\beta, \sin\beta)$.

Hence, Eq.(18) can be simplified to

$$\frac{\partial^2}{\partial x^2}\vec{\mu}_s = \frac{1}{D_s}\begin{pmatrix} (\tau_x^s)^{-1} & -\gamma_c B\sin\beta & \gamma_c B\cos\beta \\ \gamma_c B\sin\beta & (\tau_y^s)^{-1} & 0 \\ -\gamma_c B\cos\beta & 0 & (\tau_z^s)^{-1} \end{pmatrix}\vec{\mu}_s = M\vec{\mu}_s, \tag{31}$$

which has a solution of the form $\vec{\mu}_s = e^{kx}\vec{v}$, with k a scalar and $\vec{v}$ a constant vector. Thus, substituting this in Eq.(31) we get the following eigenvalue problem

$$M\vec{v}_n = k_n^2\vec{v}_n, \tag{32}$$

with $\{k_n^2, \vec{v}_n\}_{n=1}^3$ the eigendecomposition of M. The corresponding solution will be a linear combination of all the independent solutions of the form

$$\vec{\mu}_s = \sum_{n=1}^{3}\left(a_n e^{\sqrt{k^2}x} + b_n e^{-\sqrt{k^2}x}\right)\vec{v}_n, \tag{33}$$

where the constants a_n, b_n are given by the boundary conditions.

The boundary conditions are determined by the geometry of the device, in the studied case, it presents 4 different regions as seen in Fig. 6. Regions I, II and IV consist of pristine graphene, known for its isotropic behaviour ($\tau_x^s = \tau_y^s = \tau_z^s$) [RSC+16]. Regions I and II are separated by the ferromagnetic contact that injects the spin current $\vec{J}_s^{\text{inj}}$ located at $x = 0$. Region III corresponds to the proximitized region where we expect to have anisotropic spin dynamics.

Therefore, we will have solve the equations imposing the following boundary conditions

$$\left\{\begin{array}{lll} x = 0: & \vec{\mu}_s^I = \vec{\mu}_s^{II} & \vec{J}_s^I = \vec{J}_s^{II} + \vec{J}_s^{\text{inj}} \\ x = l: & \vec{\mu}_s^{II} = \vec{\mu}_s^{III} & \vec{J}_s^{II} = \vec{J}_s^{III} \\ x = l + w: & \vec{\mu}_s^{III} = \vec{\mu}_s^{IV} & \vec{J}_s^{III} = \vec{J}_s^{IV} \\ x = \pm\infty: & \vec{\mu}_s = 0 & \vec{J}_s = 0 \end{array}\right\}. \tag{34}$$

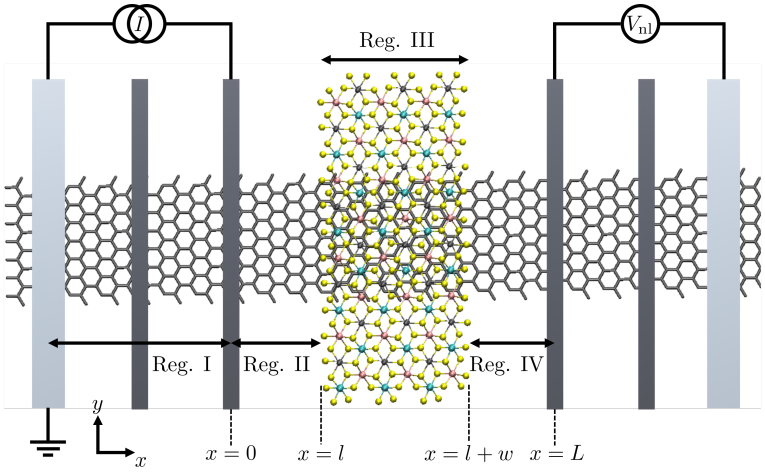

Figure 6: **Device scheme.** Proximitized spin valve with graphene/CIPS heterostructure to study spin dynamics.

4 Device fabrication and characterization

4.1 Mechanical exfoliation

Graphene, the first two-dimensional material to be obtained and characterized, was isolated by Geim and Novoselov in 2004 using mechanical exfoliation [NGM+04]. Since this milestone, mechanical exfoliation has become a widely adopted technique in laboratories to produce high-quality 2D single crystals. We will make use of this method to exfoliate both graphene and CIPS, which involves breaking the weak van der Waals forces that hold the layers of the bulk crystal together. By repeatedly peeling the material with adhesive tape, thinner flakes can be separated from the bulk, until achieving few-layer or monolayer flakes. However, overexfoliation can reduce the lateral size of the flakes, as the crystals tend to shatter during the process. Once thin layers are present on the tape, a final exfoliation step is carried out to transfer the 2D material onto a target substrate. For the graphene flakes the substrate is a heavily doped silicon wafer with a thin SiO_2 layer of 285 nm on top (SiO_2/Si^{++}). These silicon substrates are cleaned with an oxigen plasma immediately before the exfoliation to minimize the humidity and the amount of molecules on the surface. In the case of CIPS, the substrate is a polymer called polydimethylsiloxane (PDMS), which will be used for the deterministic transfer of the flake. The PDMS stamps are treated with an UV/O_3 cleaner to ensure the complete reaction of free radicals, avoiding contamination.

4.2 Characterization of the materials

The substrates with exfoliated 2D materials are examined under an optical microscope. For graphene flakes, selecting a substrate with an optimal SiO_2 thickess ensures a suitable optical contrast [LWH+13]. For CIPS, we used the microscope in transmission mode to verify the quality of the flakes.

Optical microscopy is combined with Raman spectroscopy and atomic force microscopy (AFM) to characterize the flakes obtained. For graphene, Raman peaks such as the G and $2D$ bands were monitored to confirm layer thickness and assess potential doping or strain. For CIPS, a recently studied material, we performed Raman spectroscopy to characterize the sample and compare with previous results [RCJ+23]. Atomic force microscopy provided topographic and thickness data of exfoliated flakes. The AFM scans verified layer count and uniformity in CIPS flakes and gave us a correlation between the optical image of the

flakes and their thickness. Fig. 7 shows the Raman spectra for both graphene and CIPS, and the topography of a CIPS flake.

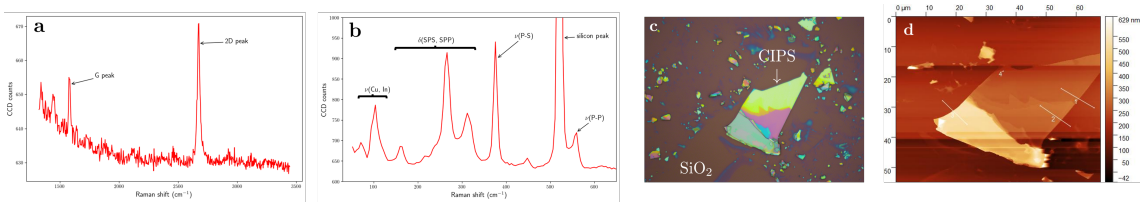

Figure 7: **Raman spectra and AFM topography. a,b.** Raman spectra of graphene and CIPS, respectively. **c,d.** Optical image and topography map obtained by AFM.

4.3 Deterministic transfer of 2D materials by all-dry viscoelastic stamping

For the transfer of the 2D materials we will follow the procedure in [CGBM+14]. This procedure is depicted in Fig. 8. Here, the PDMS with the CIPS flake is approached to the silicon substrate with the graphene flake until they are in close contact. Then, the PDMS is removed leaving the CIPS flake on the silicon substrate.

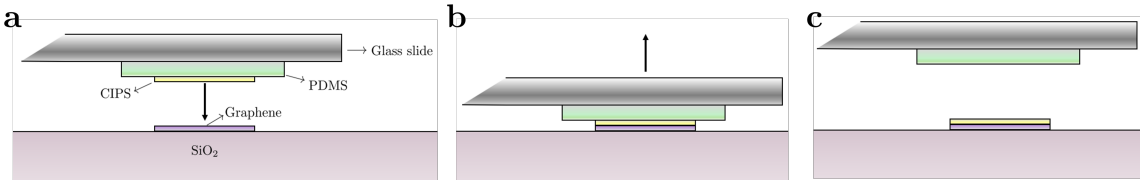

Figure 8: **All-dry viscoelastic deterministic transfer. a.** The glass slide with the PDMS having the CIPS flake is approached to the graphene flake on the SiO_2 substrate. **b.** Both flakes are put into contact. **c.** The glass slide with PDMS is removed from the substrate and the heterostructure is formed.

After the transfer, high vacuum thermal annealing is used to remove residues from the surface of the heterostructure, remaining from the previous steps, and to improve the interface quality between the flakes by reducing air and humidity molecules in between.

4.4 EBL, evaporation and wirebonding

After assembling the heterostructures, electrodes are patterned using electron-beam lithography and evaporation. A bilayer resist made of methyl methacrylate and polymethyl methacrylate (MMA/PMMA) is spin-coated, patterned with the electron-beam lithography system, and developed in methyl isobutyl ketone and isopropyl alcohol (1:3). Metal contacts are deposited via electron-beam evaporation.

Non-magnetic Ti/Pd electrodes are first defined and evaporated (2 nm of Ti and 25 nm of Pd), and contact both graphene and CIPS, as seen in Fig. 9 **b**.

For the ferromagnetic electrodes, the tunnel barrier, consisting of TiO_2, is prepared by a two-step evaporation-oxidation process. First, 4 Å thick layer of Ti is evaporated, followed by 30 min of oxidation in O_2. The process is repeated to have a tunnel barrier of approximately 8 Å. Afterward, 25 nm of Co are evaporated to give the ferromagnetic electrodes, as seen in Fig. 9 **c**. These contacts have varying widths to control magnetic switching, ranging from 140 to 180 nm.

Eventually, the resist is removed by lift-off in acetone, and the device is wire-bonded to a chip carrier and loaded into a cryostat under vacuum for measurements.

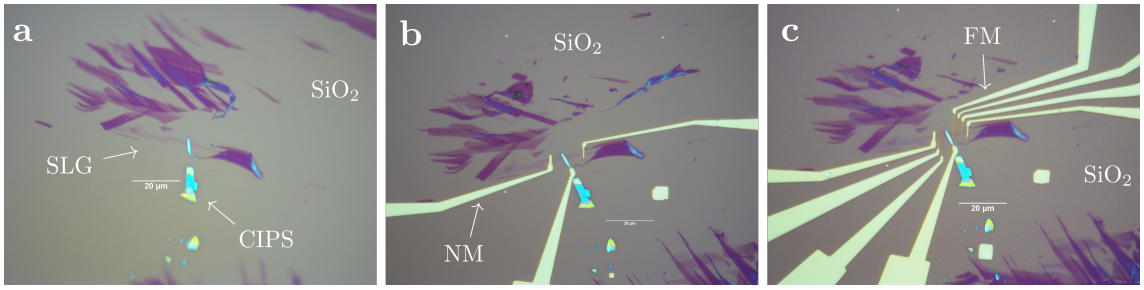

Figure 9: **Device fabrication. a.** Transferred heterostructure of single layer graphene (SLG) and CIPS on SiO_2. **b,c.** Evaporation of non-magnetic and ferromagnetic electrodes,respectively.

4.5 Measurement setup

The measurement setup included a cryostat, a switch box, an electromagnet, and a rack equipped with a temperature controller, current and voltage sources, and multimeters.

The cryostat presents a closed-cycle helium system, with high-purity helium gas circulating between a compressor and cold head to reach a base temperature of ∼5 K. A local heater allows temperature control up to room temperature.

An electrical switch box selects the measurement configuration, while grounding protects the sample from electrostatic discharge. The electromagnet, made of two coils, is mounted on a rotatory stage in low-temperature setups to precisely control the magnetic field angle relative to the ferromagnets of the device, getting up to 1 T.

4.6 Scanning Electron Microscopy

When all the measurements are done in the device, scanning electron microscopy (SEM) images are taken.

Since the lithography is never identical to the designed geometry, actual lengths are measured from the SEM images as seen in Fig. 10, to be more precise when fitting the experimental data to the analytical expressions.

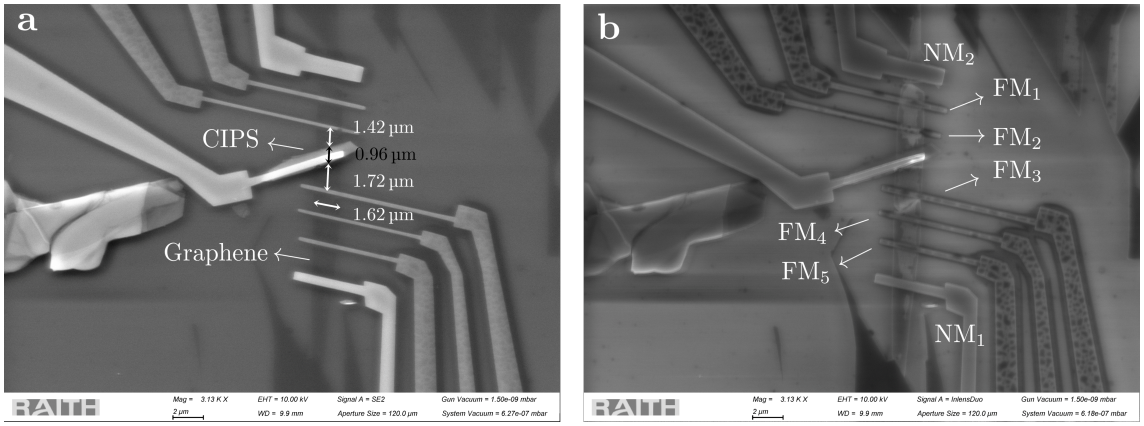

Figure 10: **SEM image of the device. a.** Secondary electrons detector image where the dimensions of the channel are depicted. **b.** Primary electrons image with FM and NM electrodes labeled; we observe the oxidation of the FM resulting in device degradation.

5 Results

Once we have the device prepared we proceed with the measurements. First of all, we do a back-gate voltage characterization to find the charge neutrality point in our sample. Then we perform Hanle spin precession experiments in the graphene reference, to extract the parameters in the isotropic case, and compare the signal with the one from the proximitized region. Afterwards, we measure oblique spin precession in both graphene and proximitized region at different back-gate voltages. Finally, we vary the top-gate and back-gate voltages to investigate the switching of CIPS, and find signatures in the transport properties of our device. We do all the experiments at different temperatures, finding that the proximity effects are more relevant at lower temperatures. The non-magnetic contacts were not operational, possibly due to the residues resulting in a poor interface quality. Therefore, only ferromagnetic contacts were used in the experiments.

5.1 Back-gate dependence

Since the device is placed on a p-doped Si/SiO_2 substrate, we can apply a back-gate voltage V_{bg}. This enables the modulation of the carrier type and density, going from holes to electrons. At the charge neutrality point, the Fermi level lies exactly at the Dirac point, where conduction and valence bands meet in graphene, meaning that there is a minimal carrier density and therefore a maximum in resistance. In a clean sample of pristine graphene, this peak should appear at zero back-gate voltage, but doping in the fabrication coming from polymers or other molecules can shift it. Hence, we inject a current and detect the voltage drop locally for each back-gate voltage applied. Moreover, we sweep the back-gate voltage back and forth to notice if there is some charge trapping, causing the charge neutrality point to move. We measure both graphene and proximitized region to see the effect of CIPS and the behaviour of the heterostructure, and the results are shown in Fig. 11. We injected current from FM_1 to FM_5, and measured the voltage drop between FM_3 and FM_4 for graphene, and between FM_2 and FM_3 for the proximitized region (see Fig. 10).

Notice in Fig. 11 **a** that the charge neutrality point of graphene is at around $V_{bg} = 30.5$ V, meaning that the sample is p-doped. We attribute this to the fact that some lithography steps were repeated several times due to a malfunctioning of the system, which forced us to spin-coat more resist onto the susbtrate resulting in a higher contamination. In Fig. 11 **b** we also observe an additional peak appearing at around $V_{bg} = -10$ V showing a hysteresis loop between the forward and the backward sweep. This behavior suggests that the hysteresis originates from the ferroelectric polarization of the CIPS layer, which can also modulate the carrier density in the graphene channel.

From this, we know if we are near to or far from the charge neutrality point when applying a certain back-gate voltage.

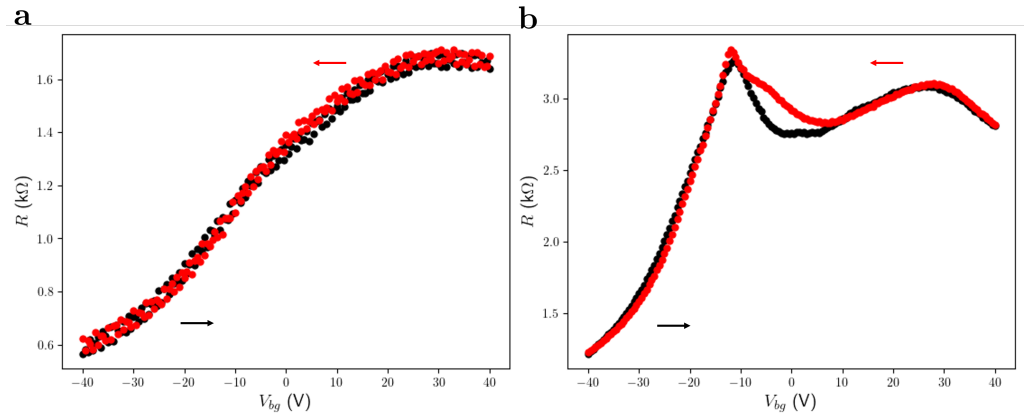

Figure 11: **Back-gate voltage dependence.** Resistance as a function of back-gate voltage for **a.** graphene and **b.** proximitized region. Black dots indicate forward sweep, while red dots correspond to backward sweep.

5.2 Hanle spin precession

The measurements of the Hanle spin precession experiment are performed at room temperature and at $T = 20$ K. We measured the graphene region as a reference, and also the whole channel with the proximitized region as seen in Fig. 12. Reference measurements were performed by injecting current from FM_4 to FM_5 and measuring the non-local voltage drop between FM_1 and FM_3. For the proximitized region, current was injected from FM_3 to FM_5 and the non-local voltage drop was measured between FM_1 and FM_2.

At room temperature, we noticed that the spin signal through the proximitized region did not present any anisotropy, result which is further confirmed in Sec. 5.3. On the other hand, to fit the data measured at $T = 20$ K we needed to introduce different spin lifetimes for the in-plane and the out-of-plane spin dynamics. Since there is isotropic in-plane transport, the behaviour for positive and negative fields is the same.

Fittings to Eq. (21) give the reference values of $\tau_s = 200$ ps at room temperature, and $\tau_s = 156$ ps at $T = 20$ K. Solutions of Eq. (31) in all regions give the values of $\tau_s = 200$ ps at room temperature. Besides, at $T = 20$ K we obtain $\tau_s = 85$ ps (graphene), and $\tau_x^s = \tau_y^s = 13$ ps and $\tau_z^s = 110$ ps (proximitized region), taking into account the tilting of the magnetization. This clearly shows that out-of-plane is the long spin lifetime direction. Additionally we extacted the polarization of the electrodes with a value of $P = 9.8\%$, which falls in the typical range $(5 - 10\%)$ [HSIA+20, SIAH+19].

To further study the out-of-plane spin lifetime anisotropy, we analyze in the next section the oblique spin precession experiment in more detail.

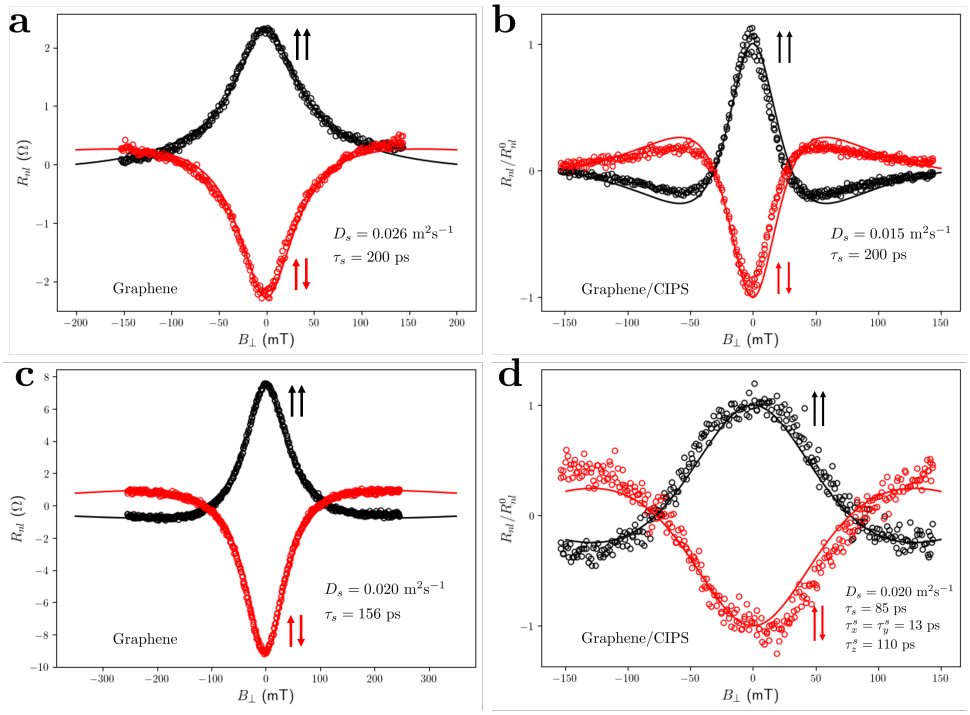

Figure 12: **Hanle spin precession measurements.** Non-local resistance as a function of the magnetic field perpendicular to the heterostructure plane at room temperature (**a**,**b**) and at $T = 20$ K (**c**,**d**). **a,c.** Measurements for the graphene region and **b,d.** for all the channel. Parallel and antiparallel configuration of injector and detector are depicted in black and red, respectively. Lines correspond to the theoretical expressions fitted for the parameters specified.

5.3 Oblique spin precession

In this section, we will discuss the experiment of oblique spin precession for both the graphene reference and the proximitized region. This experiment allows us to take the spins out-of-plane and therefore probe their out-of-plane lifetime. Measurements at room temperature and at $T = 20$ K are performed to gain deeper insight in the anisotropic spin transport.

In Fig. 13 we observe the non-local spin signal when applying a magnetic field in different directions at room temperature and with a back-gate voltage of $V_{\text{bg}} = 30$ V. Both Fig. 13 **a.** and **b.** present a similar behaviour, without showing a significant anisotropy.

On the other hand, the measurements at $T = 20$ K and with a back-gate voltage of $V_{\text{bg}} = 0$ V are shown in Fig. 14. In this case, we notice that for the proximitized region (Fig. 14 **b.**) there are angles in which the non-local resistance is larger than the signal at zero field, R_{nl}^0, indication that spin lifetimes are larger out-of-plane. This is in contrast to the pristine graphene (Fig. 14 **a.**) and the room temperature scenarios, where R_{nl}^0 was an upper limit of the resistance.

Solving for the analytical solution, we introduced an out-of-plane spin lifetime anisotropy, giving rise to a similar response in both Fig. 15 **a.** and **b.** curves.

With this, we can fit the data obtained to Eq. (28) to compare the room temperature and the $T = 20$ K cases. This analysis can be seen in Fig. 16. Fig. 16 **a.** shows that both reference and proximitized region have isotropic spin dynamics, with anisotropy ratios of $\zeta = 1.01$ and $\zeta = 1.04$, respectively.

Conversely, in Fig. 16 **b.** we observe the expected out-of-plane anisotropy of the proximitized region in comparison to the reference, as the extracted anisotropy ratios for

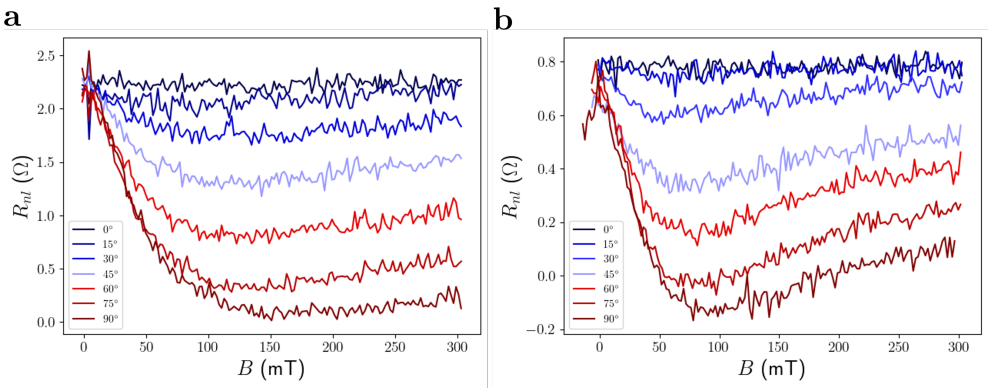

Figure 13: **Oblique spin precession at room temperature.** Non-local resistance as a function of the applied field for different directions, in **a.** graphene and **b.** the whole channel. Slight change in the shape of the curves is observed, but not a noticeable out-of-plane anisotropy.

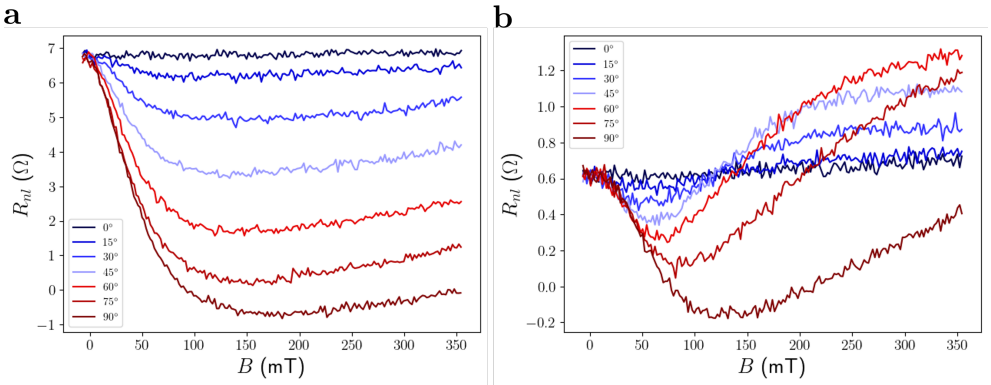

Figure 14: **Oblique spin precession at $T = 20$ K.** Non-local resistance as a function of the applied field for different directions, in **a.** graphene and **b.** the whole channel. **b.** Anisotropic out-of-plane spin transport is observed.

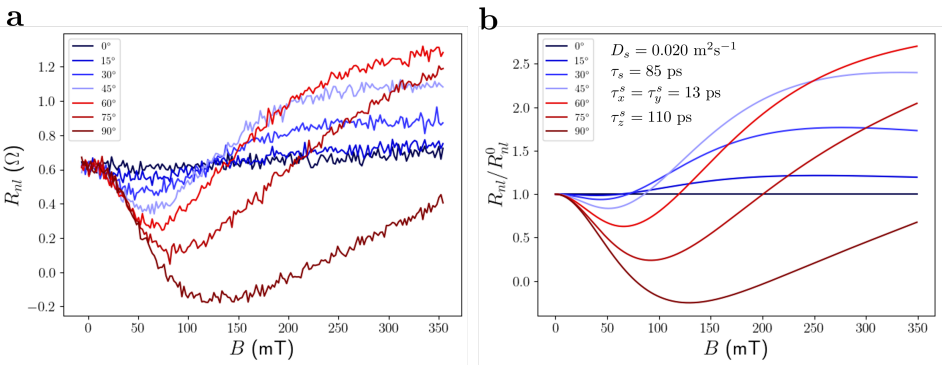

Figure 15: **Analytical curves for the oblique spin precession. a.** Experimental data of the anisotropic dynamics and **b.** theoretical curves for the specified values.

graphene and the proximitized region are $\zeta = 0.9$ and $\zeta = 6$, respectively. We consider that the reference is isotropic since the data falls in the $\zeta = 1$ line, considering the error bars. Notice that the anisotropy ratio found for the proximitized region is of the same order of magnitude as the values introduced in Fig. 15 **b.**, confirming the validity of the approximation.

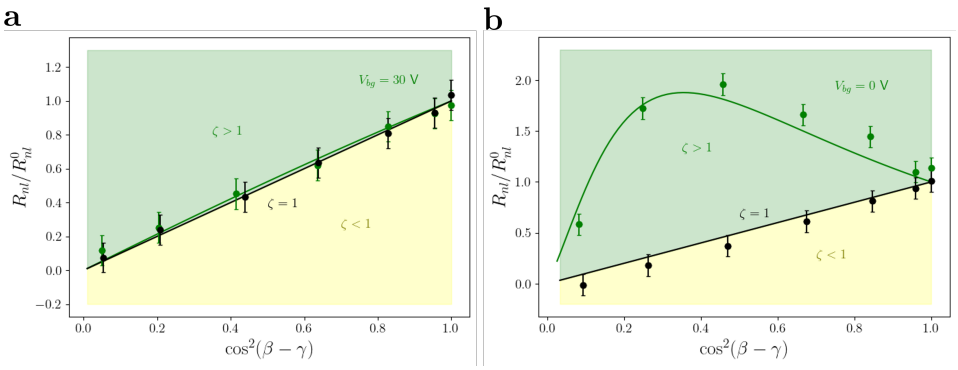

Figure 16: **Spin lifetime anisotropy, ζ.** Fitted data for **a.** room temperature and **b.** $T = 20$ K. Error bars are extracted from the noise in Fig. 13 and Fig. 14. Regions with long and short out-of-plane spin lifetime are depicted in green and yellow, respectively.

Once we demonstrated anisotropy at low temperatures, we performed a back-gate voltage characterization to see the possible anisotropy modulation. To this end, we chose different values for the back-gate voltage and did the same oblique experiment extracting the corresponding parameters. Results of these measurements are shown in Fig. 17.

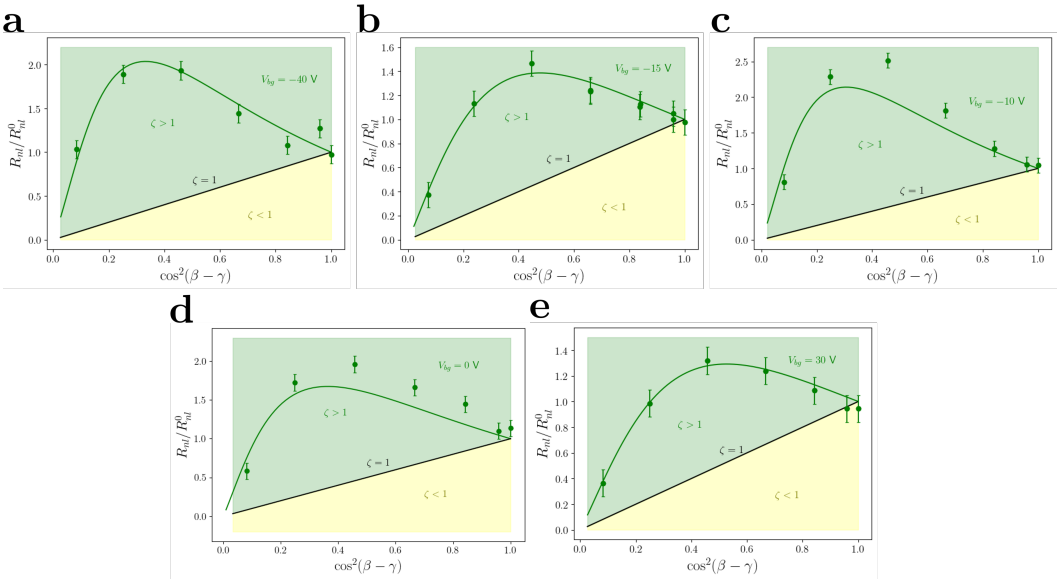

Figure 17: **Back-gate dependence of anisotropy.** Non precessing spin signal at values of the back-gate voltage of **a.** $V_{\text{bg}} = -40$ V, **b.** $V_{\text{bg}} = -15$ V, **c.** $V_{\text{bg}} = -10$ V, **d.** $V_{\text{bg}} = 0$ V, **e.** $V_{\text{bg}} = 30$ V. Notice that in **b.** there are three additional points corresponding to $\beta = -15°, -30°, -45°$.

Fitting the data we extracted the anisotropy ratio for back-gate voltages of magnitude $V_{\text{bg}} = -40, -15, -10, 0, 30$ V giving values of $\zeta = 7, 3.5, 8, 6, 3$, respectively. To see the dependence, we plotted the anisotropy ratio against the back-gate voltage, resulting in Fig. 18. We observe that the anisotropy is larger for the back-gate voltage near the hysteresis coming from CIPS. We could not see a clear trend when varying the back-gate

voltage. However, we notice a large jump in anisotropy around the region in which the CIPS hysteresis is observed (see next section).

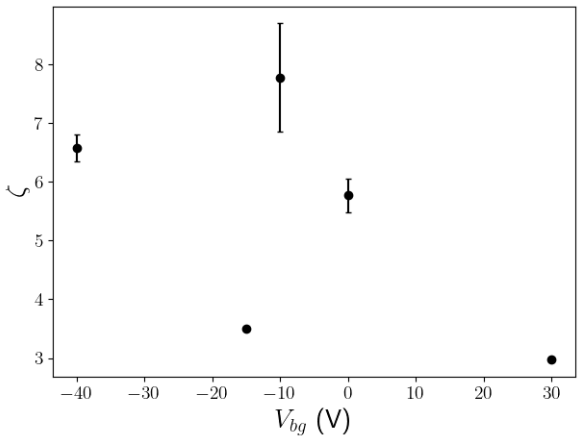

Figure 18: **Anisotropy as a function of voltage.** Error bars are extracted from the fittings in Fig. 17. Largest anisotropy is observed at $V_{\text{bg}} = -10$ V, but no clear trend is observed.

5.4 Top-gate + Back-gate characterization

Following the back-gate characterization, we also tried to study the influence of the top-gate voltage in spin dynamics. Unfortunately, the tunnel barriers suffered a lot of degradation making it impossible to inject nor detect any clean and reliable spin current.

Therefore, we decided to study how both top-gate and back-gate voltages affected the resistance of the channel. For this, we swept both voltages at different temperatures. Since we saw a hysteresis in the back-gate dependence (Fig. 11, possibly coming from switching of the polarization domains in CIPS) we expect to have a similar behavior when varying the top-gate voltage.

To determine if there are artifacts, we performed a forward and backward sweep in the top-gate voltage. Subtracting both sweeps we should see one peak coming from the hysteresis. If there is some charge trapping or inhomogeneity coming from the fabrication residues, we would observe two peaks of different sign. This is due to the fact that these trapped charges shift the local electrostatic potential, effectively doping regions of the device differently, resulting in different charge neutrality points.

The results for different temperatures are shown in Fig. 19. In dashed lines we can observe the trajectory of the hysteresis peak. When applying a back-gate voltage we shift the carrier density. To bring the system back to the same electrostatic condition (e.g., same electric field), the top-gate voltage must shift in the opposite direction. This shift is linear because the carrier density in the channel depends linearly on the capacitive coupling of both top-gate and back-gate voltages.

The slope in the trajectory varies with temperature since polarization switching is thermally activated. At low temperatures, domain switching is more difficult and requires larger gate fields. This makes the hysteresis peak shift more steeply with respect to back-gate voltage, since compensation is harder.

This result further motivates the study of the spin dynamics in this type of device, since it shows a great potential to tune the anisotropy.

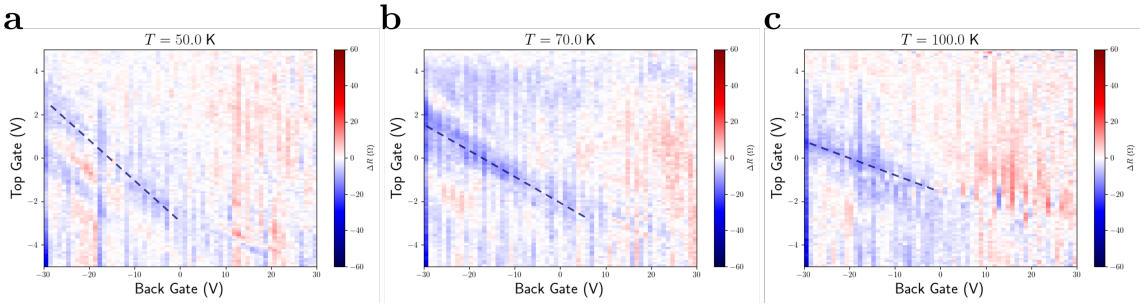

Figure 19: **Top-gate and Back-gate voltage characterization.** Resistance difference between forward and backward top-gate voltage sweeping at **a.** 50 K, **b.** 70 K and **c.** 100 K.

6 Conclusions and Outlook

Controlling spin-orbit coupling in spintronics is essential for future low-dissipation and energy-efficient information technologies. Graphene alone is ideal for spin transport due to its weak spin-orbit coupling, but it cannot be used to control and manipulate spin currents. Aiming to confere spin-orbit coupling through proximity-induced effects, other materials such as transition metal dichalcogenides are combined with graphene, showing spin lifetime anisotropy. Nevertheless, with them it is not possible to control the anisotropy in a non-volatile manner. With this goal, we fabricated a graphene spin valve lateral device proximitized with $CuInP_2S_6$, a ferroelectric 2D material. The polarization of this material lies out-of-plane, suggesting that it could tune the Rashba spin orbit field induced by the broken out-of-plane symmetry in the heterostructure. Moreover, its polarization can be switched by a local top-gate voltage, which is promising for the modulation of spin anisotropy. With the device prepared we obtained several important results:

- The back-gate dependence showed an additional peak with a hysteresis coming from CIPS.
- Theoretical analysis of spin dynamics in a proximitized spin valve lateral device with out-of-plane anisotropic spin relaxation was achieved.
- Spin lifetime anisotropy was observed at low temperatures in the fabricated device, which is a direct consequence of the imprinted spin-orbit coupling by CIPS.
- Study of the anisotropy by varying the back-gate voltage indicated that anisotropy showed a sudden change around the region in which the hysteresis appeared. However, further analysis with deterministic switching of CIPS is needed to assert whether ferroelectricity is involved.
- Characterization of the influence of both top-gate and back-gate voltages exhibited a hysteresis peak coming from CIPS, which reinforces the need to investigate spin dynamics in this type of devices.

We are confident that with future cleaner and less noisy devices we will be able to fully characterize the proximity-induced spin-orbit coupling, and also to tune the spin lifetime anisotropy by varying the carrier density of graphene and the polarization of CIPS simultaneaously. Furthermore, we should explore the possibility of having an additional in-plane anisotropy, since there are devices that have shown anisotropic spin dynamics in the three spatial dimensions [SSST+25]. Eventually, we could improve the oblique precession data analysis with other tools like machine learning, since the fittings are very sensitive to the variation of the variables and the parameter space is huge.

Bibliography

[BBF+88] M. N. Baibich, J. M. Broto, A. Fert, F. Nguyen Van Dau, F. Petroff, P. Etienne, G. Creuzet, A. Friederich, and J. Chazelas. Giant magnetoresistance of (001)Fe/(001)Cr magnetic superlattices. *Physical Review Letters*, 61(21):2472–2475, November 1988.

[BGSZ89] G. Binasch, P. Grünberg, F. Saurenbach, and W. Zinn. Enhanced magnetoresistance in layered magnetic structures with antiferromagnetic interlayer exchange. *Physical Review B*, 39(7):4828–4830, March 1989.

[BLM+15] Ganesh R. Bhimanapati, Zhong Lin, Vincent Meunier, Yeonwoong Jung, Judy Cha, Saptarshi Das, Di Xiao, Youngwoo Son, Michael S. Strano, Valentino R. Cooper, Liangbo Liang, Steven G. Louie, Emilie Ringe, Wu Zhou, Steve S. Kim, Rajesh R. Naik, Bobby G. Sumpter, Humberto Terrones, Fengnian Xia, Yeliang Wang, Jun Zhu, Deji Akinwande, Nasim Alem, Jon A. Schuller, Raymond E. Schaak, Mauricio Terrones, and Joshua A. Robinson. Recent advances in two-dimensional materials beyond graphene. *ACS Nano*, 9(12):11509–11539, November 2015.

[BSST+17] L. Antonio Benítez, Juan F. Sierra, Williams Savero Torres, Aloïs Arrighi, Frédéric Bonell, Marius V. Costache, and Sergio O. Valenzuela. Strongly anisotropic spin relaxation in graphene–transition metal dichalcogenide heterostructures at room temperature. *Nature Physics*, 14(3):303–308, December 2017.

[CGBM+14] Andres Castellanos-Gomez, Michele Buscema, Rianda Molenaar, Vibhor Singh, Laurens Janssen, Herre S J van der Zant, and Gary A Steele. Deterministic transfer of two-dimensional materials by all-dry viscoelastic stamping. *2D Materials*, 1(1):011002, April 2014.

[DFV+16] Marc Drögeler, Christopher Franzen, Frank Volmer, Tobias Pohlmann, Luca Banszerus, Maik Wolter, Kenji Watanabe, Takashi Taniguchi, Christoph Stampfer, and Bernd Beschoten. Spin lifetimes exceeding 12 ns in graphene nonlocal spin valve devices. *Nano Letters*, 16(6):3533–3539, May 2016.

[DMG98] Eric D. Daniel, C. Denis Mee, and Mark Griffiths, editors. *Magnetic Recording: The First 100 Years*. IEEE Press, New York, 1998.

[GF15] Martin Gmitra and Jaroslav Fabian. Graphene on transition-metal dichalcogenides: A platform for proximity spin-orbit physics and optospintronics. *Phys. Rev. B Condens. Matter Mater. Phys.*, 92(15), October 2015.

[GKE+09] M. Gmitra, S. Konschuh, C. Ertler, C. Ambrosch-Draxl, and J. Fabian. Band-structure topologies of graphene: Spin-orbit coupling effects from first principles. *Physical Review B*, 80(23), December 2009.

[GKF13] Martin Gmitra, Denis Kochan, and Jaroslav Fabian. Spin-orbit coupling in hydrogenated graphene. *Physical Review Letters*, 110(24), June 2013.

[GKHF16] Martin Gmitra, Denis Kochan, Petra Högl, and Jaroslav Fabian. Trivial and inverted dirac bands and the emergence of quantum spin hall states in graphene on transition-metal dichalcogenides. *Physical Review B*, 93(15), April 2016.

[GPS+19] Z M Gebeyehu, S Parui, J F Sierra, M Timmermans, M J Esplandiu, S Brems, C Huyghebaert, K Garello, M V Costache, and S O Valenzuela. Spin communication over 30 µm long channels of chemical vapor deposited graphene on SiO_2. *2D Materials*, 6(3):034003, May 2019.

[HJ70] Thomas G. Halley and Reynold B. Johnson. Magnetic disk memory, March 1970. United States Patent US3503060A.

[HSIA+20] Franz Herling, C. K. Safeer, Josep Ingla-Aynés, Nerea Ontoso, Luis E. Hueso, and Fèlix Casanova. Gate tunability of highly efficient spin-to-charge conversion by spin hall effect in graphene proximitized with WSe_2. *APL Materials*, 8(7), July 2020.

[JHF+02] F. J. Jedema, H. B. Heersche, A. T. Filip, J. J. A. Baselmans, and B. J. van Wees. Electrical detection of spin precession in a metallic mesoscopic spin valve. *Nature*, 416(6882):713–716, April 2002.

[JS85] Mark Johnson and R. H. Silsbee. Interfacial charge-spin coupling: Injection and detection of spin magnetization in metals. *Physical Review Letters*, 55(17):1790–1793, October 1985.

[JS88a] Mark Johnson and R. H. Silsbee. Coupling of electronic charge and spin at a ferromagnetic-paramagnetic metal interface. *Physical Review B*, 37(10):5312–5325, April 1988.

[JS88b] Mark Johnson and R. H. Silsbee. Spin-injection experiment. *Physical Review B*, 37(10):5326–5335, April 1988.

[LWH+13] Hai Li, Jumiati Wu, Xiao Huang, Gang Lu, Jian Yang, Xin Lu, Qihua Xiong, and Hua Zhang. Rapid and reliable thickness identification of two-dimensional nanosheets using optical microscopy. *ACS Nano*, 7(11):10344–10353, October 2013.

[LYS+16] Fucai Liu, Lu You, Kyle L. Seyler, Xiaobao Li, Peng Yu, Junhao Lin, Xuewen Wang, Jiadong Zhou, Hong Wang, Haiyong He, Sokrates T. Pantelides, Wu Zhou, Pradeep Sharma, Xiaodong Xu, Pulickel M. Ajayan, Junling Wang, and Zheng Liu. Room-temperature ferroelectricity in $CuInP_2S_6$ ultrathin flakes. *Nature Communications*, 7(1), August 2016.

[MCS+97] V. Maisonneuve, V. B. Cajipe, A. Simon, R. Von Der Muhll, and J. Ravez. Ferrielectric ordering in lamellar title $CuInP_2S_6$. *Physical Review B*, 56(17):10860–10868, November 1997.

[MNL+18] Sasikanth Manipatruni, Dmitri E. Nikonov, Chia-Ching Lin, Tanay A. Gosavi, Huichu Liu, Bhagwati Prasad, Yen-Lin Huang, Everton Bonturim, Ramamoorthy Ramesh, and Ian A. Young. Scalable energy-efficient magnetoelectric spin–orbit logic. *Nature*, 565(7737):35–42, December 2018.

[MVSK17] Sadamichi Maekawa, Sergio O. Valenzuela, Eiji Saitoh, and Takashi Kimura. *Spin Current*. Oxford University Press, 09 2017.

[NGM+04] K. S. Novoselov, A. K. Geim, S. V. Morozov, D. Jiang, Y. Zhang, S. V. Dubonos, I. V. Grigorieva, and A. A. Firsov. Electric field effect in atomically thin carbon films. *Science*, 306(5696):666–669, October 2004.

[Ras00] E. I. Rashba. Theory of electrical spin injection: Tunnel contacts as a solution of the conductivity mismatch problem. *Physical Review B*, 62(24):R16267–R16270, December 2000.

[RCJ+23] Rahul Rao, Benjamin S. Conner, Jie Jiang, Ruth Pachter, and Michael A. Susner. Raman spectroscopy study of pressure-induced phase transitions in single crystal cuinp2s6. *The Journal of Chemical Physics*, 159(22), December 2023.

[RSC+16] Bart Raes, Jeroen E. Scheerder, Marius V. Costache, Frédéric Bonell, Juan F. Sierra, Jo Cuppens, Joris Van de Vondel, and Sergio O. Valenzuela. Determination of the spin-lifetime anisotropy in graphene using oblique spin precession. *Nature Communications*, 7(1), May 2016.

[SFK+21] Juan F. Sierra, Jaroslav Fabian, Roland K. Kawakami, Stephan Roche, and Sergio O. Valenzuela. Van der waals heterostructures for spintronics and opto-spintronics. *Nature Nanotechnology*, 16(8):856–868, July 2021.

[SFM+00] G. Schmidt, D. Ferrand, L. W. Molenkamp, A. T. Filip, and B. J. van Wees. Fundamental obstacle for electrical spin injection from a ferromagnetic metal into a diffusive semiconductor. *Physical Review B*, 62(8):R4790–R4793, August 2000.

[SIAH+19] C. K. Safeer, Josep Ingla-Aynés, Franz Herling, José H. Garcia, Marc Vila, Nerea Ontoso, M. Reyes Calvo, Stephan Roche, Luis E. Hueso, and Fèlix Casanova. Room-temperature spin hall effect in graphene/mos2 van der waals heterostructures. *Nano Letters*, 19(2):1074–1082, January 2019.

[SNC+17] Juan F. Sierra, Ingmar Neumann, Jo Cuppens, Bart Raes, Marius V. Costache, and Sergio O. Valenzuela. Thermoelectric spin voltage in graphene. *Nature Nanotechnology*, 13(2):107–111, December 2017.

[SRM+94] A. Simon, J. Ravez, V. Maisonneuve, C. Payen, and V. B. Cajipe. Paraelectric-ferroelectric transition in the lamellar thiophosphate $CuInP_2S_6$. *Chemistry of Materials*, 6(9):1575–1580, September 1994.

[SSST+25] Juan F. Sierra, Josef Světlík, Williams Savero Torres, Lorenzo Camosi, Franz Herling, Thomas Guillet, Kai Xu, Juan Sebastián Reparaz, Vera Marinova, Dimitre Dimitrov, and Sergio O. Valenzuela. Room-temperature anisotropic in-plane spin dynamics in graphene induced by $PdSe_2$ proximity. *Nature Materials*, 24(6):876–882, February 2025.

[SW48] E.C. Stoner and E.P. Wohlfarth. A mechanism of magnetic hysteresis in heterogeneous alloys. *Philosophical Transactions of the Royal Society of London. Series A, Mathematical and Physical Sciences*, 240(826):599–642, May 1948.

[TG08] C Tannous and J Gieraltowski. The Stoner–Wohlfarth model of ferromagnetism. *European Journal of Physics*, 29(3):475–487, March 2008.

[TJP+07] Nikolaos Tombros, Csaba Jozsa, Mihaita Popinciuc, Harry T. Jonkman, and Bart J. van Wees. Electronic spin transport and spin precession in single graphene layers at room temperature. *Nature*, 448(7153):571–574, July 2007.

[VBS+22] Frank Volmer, Timo Bisswanger, Anne Schmidt, Christoph Stampfer, and Bernd Beschoten. Charge-induced artifacts in nonlocal spin-transport measurements: How to prevent spurious voltage signals. *Physical Review Applied*, 18(1), July 2022.

[VT06] S. O. Valenzuela and M. Tinkham. Direct electronic measurement of the spin hall effect. *Nature*, 442(7099):176–179, July 2006.

[ZJNF23] Klaus Zollner, Simão M. João, Branislav K. Nikolić, and Jaroslav Fabian. Twist- and gate-tunable proximity spin-orbit coupling, spin relaxation anisotropy, and charge-to-spin conversion in heterostructures of graphene and transition metal dichalcogenides. *Physical Review B*, 108(23), December 2023.

[ZKGF25] Klaus Zollner, Marcin Kurpas, Martin Gmitra, and Jaroslav Fabian. First-principles determination of spin–orbit coupling parameters in two-dimensional materials. *Nature Reviews Physics*, 7(5):255–269, March 2025.

[ŽMAS+19] Igor Žutić, Alex Matos-Abiague, Benedikt Scharf, Hanan Dery, and Kirill Belashchenko. Proximitized materials. *Materials Today*, 22:85–107, January 2019.

A Derivations

A.1 Isotropic Hanle spin precession curve

In this experiment we inject a spin current $\vec{\mu}_s$ polarized in the y direction, and we apply a perpendicular magnetic field $\vec{B} = B\hat{z}$. The Bloch diffusion equation reads

$$\frac{\partial}{\partial t}\vec{\mu}_s = D_s\frac{\partial^2}{\partial x^2}\vec{\mu}_s - \omega_L\vec{\mu}_s \times \hat{z} - \frac{\vec{\mu}_s}{\tau_s} \tag{35}$$

Therefore, spins will precess in the xy plane, so we will ignore μ_z^s. Defining $\vec{\mu}_\perp = (\mu_x, \mu_y)$ we can write

$$\frac{\partial}{\partial t}\vec{\mu}_\perp = D_s\frac{\partial^2}{\partial x^2}\vec{\mu}_\perp + \begin{pmatrix} -\frac{1}{\tau_s} & \omega_L \\ -\omega_L & -\frac{1}{\tau_s} \end{pmatrix}\vec{\mu}_\perp \tag{36}$$

.

If we perform the Fourier transform of $\vec{\mu}_\perp(k,t)$

$$\vec{\mu}_\perp(k,t) = \int_{-\infty}^{\infty} e^{-ikx}\vec{\mu}_\perp(x,t)dx, \tag{37}$$

we can express Eq.(36) as

$$\frac{\partial}{\partial t}\vec{\mu}_\perp(k,t) = \begin{pmatrix} -D_sk^2 - \frac{1}{\tau_s} & \omega_L \\ -\omega_L & -D_sk^2 - \frac{1}{\tau_s} \end{pmatrix}\vec{\mu}_\perp(k,t) = M(k)\vec{\mu}_\perp(k,t). \tag{38}$$

Hence, the solution is of the form

$$\vec{\mu}_\perp(k,t) = e^{M(k)t}\vec{\mu}_\perp(k,0) \tag{39}$$

For the initial condition:

$$\vec{\mu}_\perp(x,0) = \mu_0\delta(x)\begin{pmatrix}0\\1\end{pmatrix} \implies \vec{\mu}_\perp(k,0) = \mu_0\begin{pmatrix}0\\1\end{pmatrix}, \tag{40}$$

where μ_0 is the magnitude of the initial spin electrochemical potential. Thus, we obtain

$$\vec{\mu}_\perp(k,t) = \mu_0 e^{M(k)t}\begin{pmatrix}0\\1\end{pmatrix}. \tag{41}$$

Diagonalizing $M(k)$ we get the eigenvalues $\lambda_\pm = -D_sk^2 - \frac{1}{\tau_s} \pm i\omega_L$. Since the detector is also polarized in y, the signal will be related to μ_y^s:

$$\mu_y^s(k,t) = \mu_0 e^{-(D_sk^2+\frac{1}{\tau_s})t}\cos(\omega_L t). \tag{42}$$

Performing the inverse Fourier transform we get the real space solution

$$\begin{aligned}\mu_y^s(x,t) &= \frac{1}{2\pi}\int_{-\infty}^{\infty} e^{ikx}\mu_0 e^{-(D_sk^2+\frac{1}{\tau_s})t}\cos(\omega_L t)dk \\ &= \mu_0\frac{1}{\sqrt{4\pi D_s t}}\exp\left(-\frac{x^2}{4D_s t}\right)\cos(\omega_L t)\exp\left(-\frac{t}{\tau_s}\right)\end{aligned} \tag{43}$$

Then we can compute the steady state spin accumulation at a distance L, where the detector is placed:

$$\mu_y^s(L) = \mu_0\int_0^{\infty}\frac{1}{\sqrt{4\pi D_s t}}\exp\left(-\frac{L^2}{4D_s t}\right)\cos(\omega_L t)\exp\left(-\frac{t}{\tau_s}\right)dt. \tag{44}$$

Notice that the initial spin electrochemical potential can be related to the spin polarized current in the injector $P_i I$ and the density of states per unit area $N(E_F)W$, where W is the width of the graphene channel, as follows

$$\mu_0 = \frac{P_i I}{eN(E_F)W} \tag{45}$$

Moreover, the spin electrochemical potential at the detector can be converted into a voltage as

$$V_{\mathrm{nl}} = \frac{P_d}{2e}\mu_y^s(L), \tag{46}$$

where P_d is the polarization of the detector. Eventually, the spin signal expressed as a non-local resistance (V_{nl}/I) can be expressed as

$$R_{\mathrm{nl}}(B) = \pm\frac{P_i P_d}{e^2 N(E_F)W}\int_0^\infty \frac{1}{\sqrt{4\pi D_s t}}\exp\left(-\frac{L^2}{4D_s t}\right)\cos(\omega_L t)\exp\left(-\frac{t}{\tau_s}\right)dt, \tag{47}$$

where $\pm$ corresponds to P and AP configurations of the ferromagnetic contacts.

A.2 Tilting of the ferromagnetic electrodes

We can model the tilting of the ferromagnets using the Stoner-Wohlfarth model [TG08, SW48], which assumes that the ferromagnet is a single magnetic domain with uniaxial anisotropy and the magnetization M is constant in magnitude rotating coherently. This model defines the magnetic energy in the following way

$$E(\gamma) = \frac{MB_s}{2}\sin^2\gamma - MB\cos(\beta-\gamma), \tag{48}$$

where the first term is the uniaxial anisotropy energy, which is lowest when the magnetization aligns with the easy axis of the ferromagnet, and the second term is the Zeeman energy. Here B_s is the saturation magnetic field, the field required to fully align the magnetization with it. Minimizing this energy and assuming that the system is in the low field limit (γ small), we obtain the following expression for the tilting

$$\gamma = \arcsin\left(\frac{B\sin\beta}{B_s + B\cos\beta}\right). \tag{49}$$